Materials Research. 2025; 28:e20240479
DOI: https://doi.org/10.1590/1980-5373-MR-2024-0479

Preparation of Negative Poisson's Ratio 316L Stainless Steel Porous Bone Scaffolds Based on Finite Element Analysis and 3D Printing Technology

***Shubo Xu*[a,b*], *Xue Yang*[a], *Xinzhi Hu*[a], *Hailong Ma*[a], *Jianing Li*[a], *Guocheng Ren*[a]**

[a]*Shandong Jianzhu University, School of Materials Science and Engineering, 250101, Jinan, China.*
[b]*Huazhong University of Technology, State Key Laboratory of Material Forming and Mould & Die Technology, 430025, Wuhan, China.*

Received: October 23, 2024; Revised: January 03, 2025; Accepted: February 02, 2025

In this paper, four negative re-entrant hexagonal honeycomb (NRHH) porous scaffolds with different extension angles θ (15°, 30°, 45° and 60°) cell structures were designed and their preparation was accomplished by selective laser melting (SLM) in 3D printing technology so that Negative Poisson Ratio metamaterials could be applied to bone implants to treat bone defects. The effects of structural design on residual stress, surface roughness, and compressive properties of NRHH porous scaffolds were evaluated by finite element analysis and experimental analysis. The results showed that the 15°-NRHH porous scaffold exhibited optimal performance. When the θ angle increased, the scaffold introduced increased residual stresses, increased surface roughness, generated increased deformation, stress, and strain, and decreased compressive performance.

Keywords: *3D printing, NPR metamaterial, porous bone scaffolds, residual stress, forming quality.*

1. Introduction

Bone defects are common in orthopaedics and larger bone defects require external intervention[1]. In recent years, a large number of metallic bone implants have been widely used in clinical practice as substitutes for bone defects. However, there are always some shortcomings in clinical outcomes compared to natural bone[2], which require optimization in the structural design and material selection of artificial bone implants. Emerging metamaterials provide a new avenue for developing materials with advanced functionality, and metamaterials intended for biomedical applications are referred to as "meta-biomaterials"[3]. Negative Poisson Ratio (NPR) materials, as one of the metamaterials, have significant mechanical property advantages including energy absorption[4], high toughness, negative Poisson's ratio[5], and light density[6,7], which provide extraordinary performance in biomedical applications[8].

Metamaterials that exhibit a Negative Poisson Ratio are known as auxiliary materials and unlike conventional materials, they contract laterally rather than expand when compressed[9]. Rocks[10], woods[11], and single crystals[12] are natural NPR metamaterials, and it has also been found that specific structural designs can lead to negative Poisson ratio properties. 2D Re-entrant structures[13], 3D Re-entrant structures[14], Star Re-entrant structures[15], Chiral structures[16], Rotating-rigid units[17,18] etc. have been proposed. In this paper, negative re-entrant hexagonal honeycomb (NRHH) structures with negative Poisson's ratio properties are used for the preparation of bone implants. Evans et al.[19] first proposed a 3D orthogonal negative Poisson's ratio structure of an NRHH. Kolken et al.[20] combined a negative Poisson's ratio structure with a positive Poisson's ratio structure to design a hybrid implant with positive and negative Poisson's ratio for hip implantation, which prolongs the life of the implant.

Additive manufacturing (AM), also known as 3D printing assists in the preparation of NRHH structures. AM technology has been widely used to build NPR metamaterials such as re-entrant[21], chiral[22], and missing ribs[23] structures.

SLM is used as an AM technique for structural design with the help of modeling software. Its high degree of design freedom presents complexity in the properties of porous scaffolds[24], and the porosity[25], pore size[26], and shape[27] of the structures are related to the mechanical properties and biocompatibility of the porous scaffolds. Deng et al.[28] showed that the geometry of porous scaffolds affected vascular growth and nutrient transport. Lu et al.[29] showed by finite element analysis and experimental analysis that pore size and scaffold geometry affect the compressive strength and elastic modulus of porous scaffolds. Therefore, the structural design of porous scaffolds is crucial to their performance.

As one of the commonly used biomaterials for metal additive manufacturing, 316L stainless steel has excellent mechanical properties, corrosion resistance, and relatively good biocompatibility[30], and is widely used for the preparation of joint replacements and other implants[31].In this paper, 316L NRHH porous bone scaffolds with negative Poisson's ratio were prepared based on the negative re-entrant hexagonal honeycomb structure by SLM, and four NRHH porous scaffolds with different cell structures were designed to observe the forming quality of SLM porous scaffolds. The relationship

*e-mail: xsb@sdjzu.edu.cn

between different structural designs and the residual stress, surface roughness, and compressive properties of the porous scaffolds is also discussed.

2. Materials and Methods

2.1. Structural design

NRHH structure is opposite to the conventional structure, when the scaffold is compressed, radial contraction and axial concavity, this property makes the aggregated density of the scaffold increase with compression, thus causing enhanced compressive properties and facilitating scaffold implantation. In order to evaluate the effect of Poisson's ratio on the mechanical properties of the porous skeletal scaffolds, four NRHH porous skeletal scaffolds with different θ-angles were designed by using NX12.0 (Siemens PLM Software, USA) software, and struts with a diameter of 400 μm were selected, and the schematic diagrams of the expanded three-dimensional structures are shown in Figure 1, and the specific design parameters are shown in Table 1, which lists the design parameters using the theoretical Poisson's ratios ν_y and ν_z calculated using Equations (2.1) and (2.2), which assumes that there are enough unit structures to ignore the edge effects, but in practice the unit structures are limited and the actual Poisson's ratios are affected by the edge effects.

$$v_y = \frac{-\cos^2\theta}{\left(\frac{a}{b}-\sin\theta\right)\sin\theta} \tag{2.1}$$

$$v_z = -\frac{\left(\frac{a}{b}-\sin\theta\right)\sin\theta}{\cos^2\theta} \tag{2.2}$$

Porosity is defined as the percentage of pore space in a solid structure. The porous skeletal scaffolds were separated from the substrate using EDM wire cutting, and then the porous skeletal scaffold samples were ultrasonically cleaned and dried, and then the mass m of the porous skeletal scaffolds was read using an electronic balance, the actual volume VP of the porous skeletal scaffolds was measured using the Archimedes drainage method, and the porosity, Porosity, was calculated from Equation 2.3.

$$Porosity = \left(1-\frac{V_P}{V_S}\right)\times 100\% \tag{2.3}$$

Where V_P is the volume of the porous structure and V_S is the volume of the dense structure.

Numerous studies have shown that porous implants with a pore size of 400-700 μm and a porosity of 30-95% are sufficiently effective for new bone growth and angiogenesis[32]. The porosity of the porous scaffolds in this study was designed to be 75%. The porous skeletal scaffolds were prepared with the process parameters: P=100W, V=600mm/s, S=0.1mm, P=0.03mm with Y-axis and Z-axis as the construction direction, respectively, and after the completion of the preparation, the porous skeletal scaffolds were separated from the substrate by EDM wire cutting, and then the porous skeletal scaffolds were cleaned by immersing them into 96% ethanol to remove some of the easily removable unfused powder, and then ultrasonically cleaned to remove the residual powder between pores through ultrasonic vibration to remove the remaining powder remaining between the pores. The eight porous skeletal scaffolds prepared by SLM are shown in Figure 2. Group A was shaped with the Y-axis as the construction direction, and they were named A15, A30, A45, and A60, at which time the theoretical Poisson's ratio $\nu = \nu_y$, and the porous skeletal scaffolds with smaller θ-angles showed greater negative Poisson's ratios; Group B was shaped with the Z-axis as the construction direction, and they were named as B15, B30, B45, B60, at this time the theoretical Poisson's ratio $\nu = \nu_z$, the porous skeletal scaffolds with larger θ-angle show greater negative Poisson's ratio.

2.2. Finite element numerical analysis

Ansys was used to carry out static analysis of NRHH porous scaffolds. Hexahedral meshing was used, and the mesh size was 0.05 mm. The boundary conditions were consistent with the compression experiments, the calculated load was an axial downward compression force of 3000N, and the boundary conditions at the bottom of the model were set to be completely constrained.

MSC Simufact Additive was used to simulate the forming process of NRHH porous scaffolds, based on the inherent strain theory to simulate the residual stress generated by the forming of NRHH porous scaffolds at different angles and with different process parameters, the model consists of 2×2×2 cells, with a mesh size of 0.06mm.

2.3. Microstructure characterization and residual stress testing

The 316L NRHH porous scaffolds were tested for residual stress using X-ray diffraction (Proto, Canada). The morphology of the porous scaffolds was characterized using a scanning electron microscope (SEM) (SUPRA

Table 1. Structural design parameters of the NRHH porous scaffolds.

θ	*a* (mm)	*b* (mm)	Pore size (μm)	ν_y	ν_z	Size(mm^3)
15°	1.600	1.035	649	-2.800	-0.357	10×10×10.6
30°	2.000	1.155	383	-1.218	-0.821	10×10×11.4
45°	3.000	1.414	434	-0.500	-2.000	10×10×12.0
60°	4.738	2.000	398	-0.192	-5.206	10×10×11.7

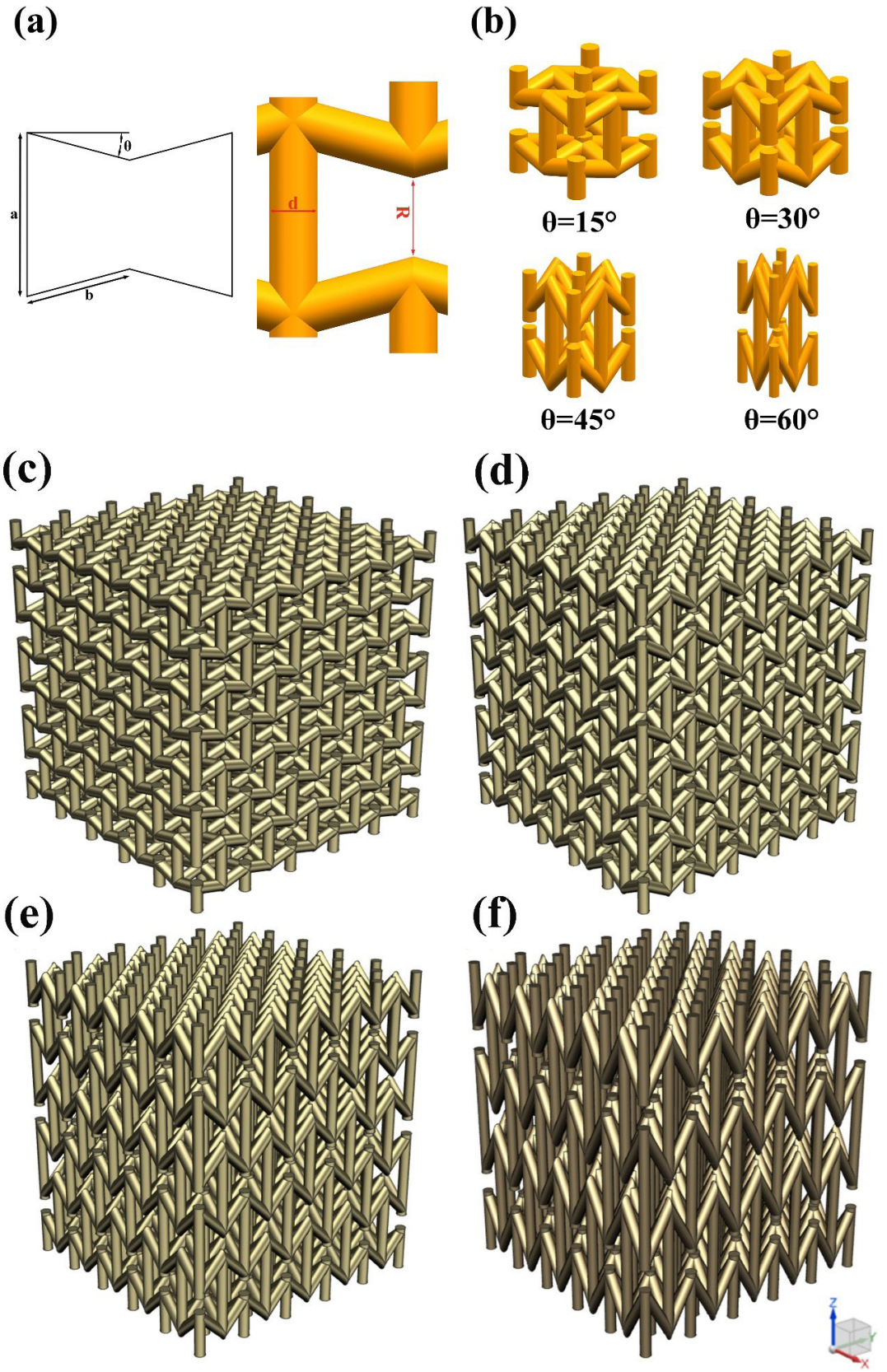

Figure 1. Schematic design parameters of NRHH porous scaffolds: (a) NPR structural design with concave angle θ and length ratio a/b and schematic diagram of scaffold spore size and strut diameter;(b)Single-unit NRHH Porous Stent Model; Model drawing of the NRHH porous scaffolds design: (c) 15°-NRHH; (d) 30°-NRHH; (e) 45°- NRHH; (f) 60°-NRHH.

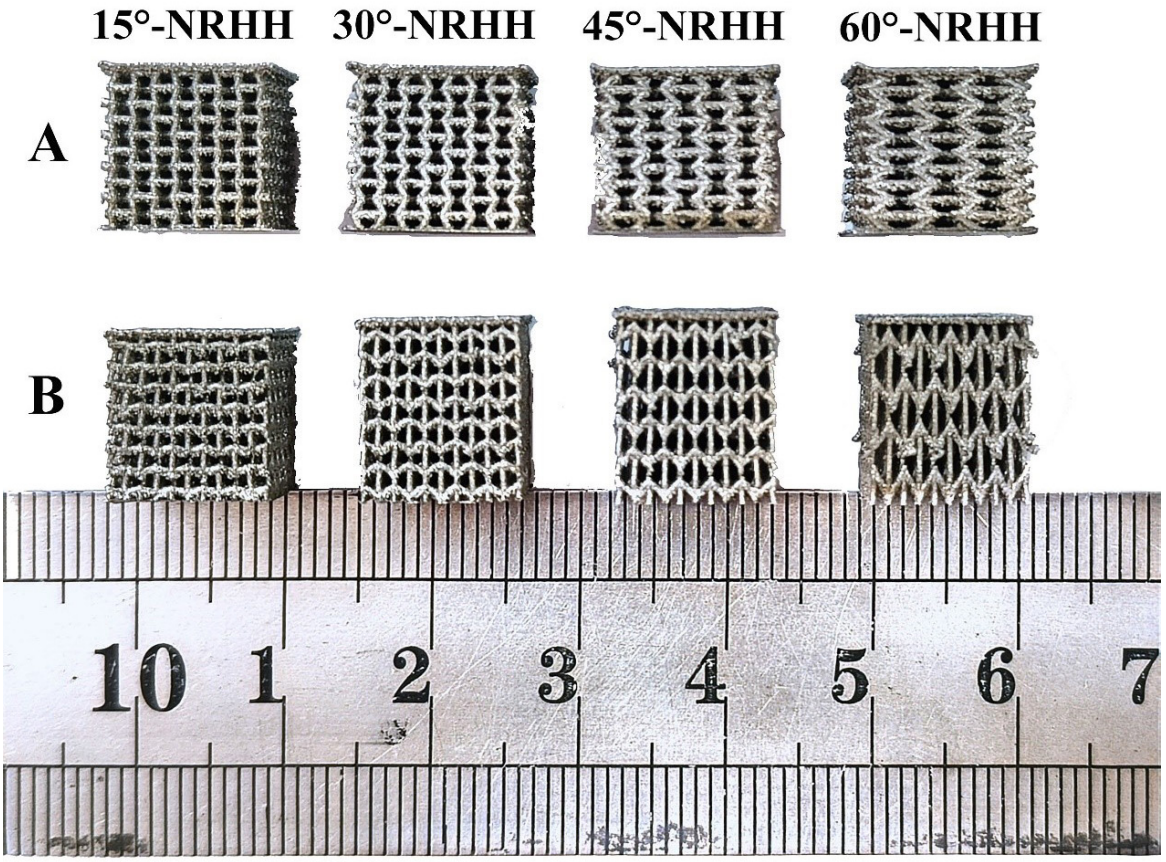

Figure 2. SLM prepared porous skeletal scaffolds with different structures of NRHH, group A was molded with Y-axis as the construction direction and group B was molded with Z-axis as the construction direction.

55, Zeiss). The surface morphology of the samples was characterized using a laser spectroscopic confocal microscope (KC-H020) with a measurement area of approximately 6 mm × 6 mm, a scanning spacing of 6 μm, a sampling frequency of 3000 Hz, and a scanning speed of 9,000 μm/s, and the line roughness Ra of the NRHH porous scaffolds was measured.

2.4. Mechanical properties

The compressive properties of the porous scaffolds were evaluated using a compressive test, which was carried out using a WDW-100E electronic universal testing machine. Axial compression was carried out using a speed of 1 mm/min and the deformation was stopped at about 70%.

3. Results and Discussion

3.1. Residual stress and residual deformation

Mercelis and Kruth[33] proposed a mechanism to explain the formation of residual stress based on the temperature gradient mechanism (TGM) model. Measurement of localized residual stress in scaffolds is difficult and requires several advanced methods, including advanced sample preparation and data analysis using X-ray or neutron techniques. In this paper, the residual stress generated during the forming process of NRHH porous scaffolds was first analyzed by finite element analysis (FEA) using MSC Simufact Additive, and then a non-destructive measurement method was chosen to test the residual stress at the intersection of the struts of 316L NRHH porous scaffolds using X-ray diffraction.

Figure 3 shows the residual stress clouds of the NRHH porous skeletal scaffolds molded in the Y-axis and Z-axis as the construction direction, respectively. From the final residual stress cloud plots in Figure 3 (a), (b), (c), (d), collectively, the porous skeletal scaffolds molded in the Y-axis as the construction direction produced significantly higher residual stresses with increasing θ-angle, and produced relatively lower residual stresses for A15 and A30 compared to A45 and A60, with the lowest residual stresses produced by A15. Figure 3. Residual stress results in (e), (f), (g), and (h) show that group B porous skeletal scaffolds formed with Z-axis as the construction direction produced relatively low residual stresses compared to group A. Residual stresses increased with increasing θ-angle for B30, B45, and B60 porous skeletal scaffolds, but the B15 porous skeletal scaffolds produced the highest residual stress (397.38 MPa).

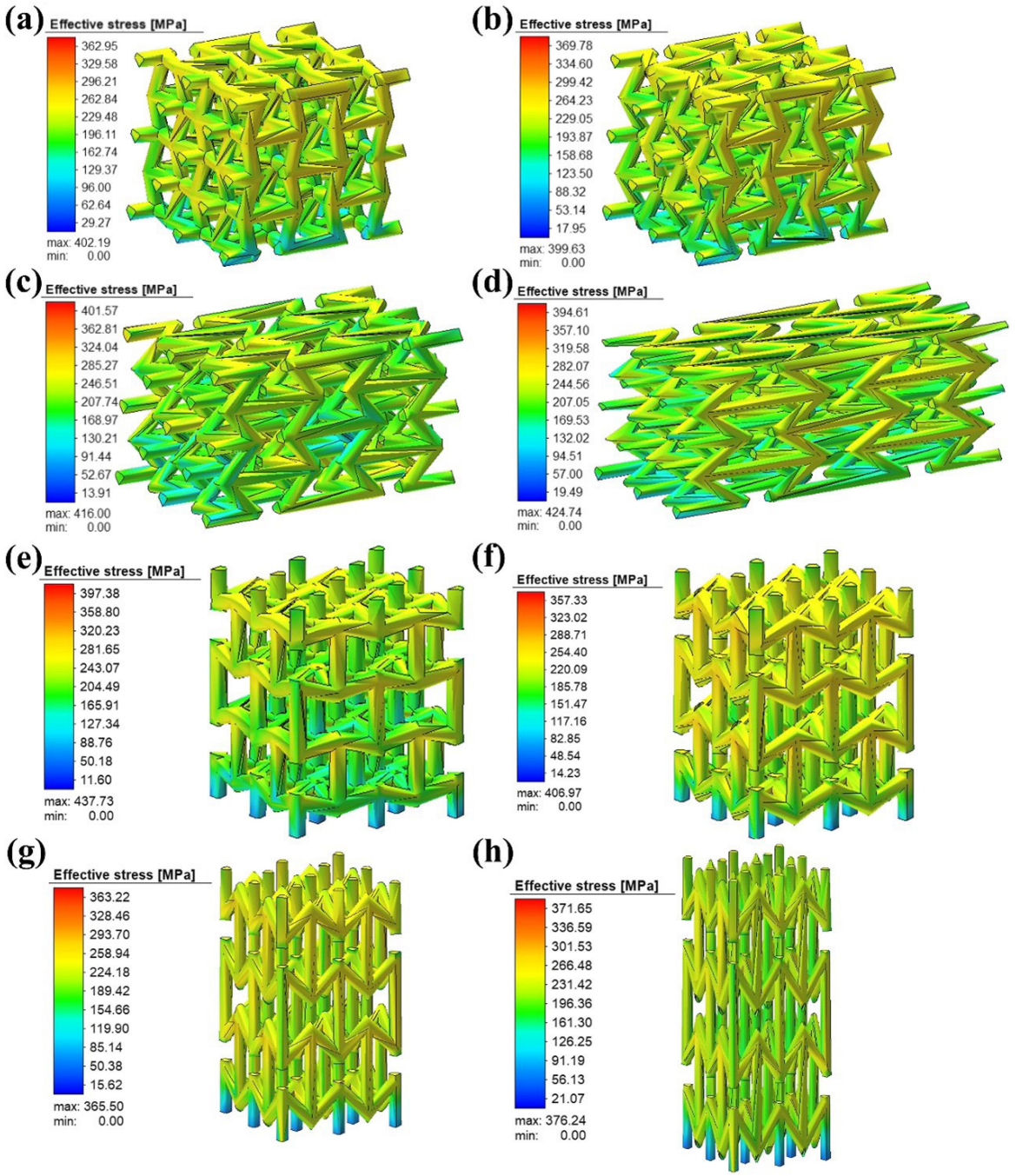

Figure 3. Final stress clouds for different structures of NRHH porous skeletal scaffolds (a) A15, (b) A30, (c) A45, (d) A60, (e) B15, (f) B30, (g) B45, (h) B60.

Figure 4 shows the experimental test values of residual stresses of the eight NRHH porous skeletal scaffolds with the test location at the intersection of the struts. The experimental test results show that the existent stresses in the scaffolds are compressive stresses, and there is a consistency between the experimental test values and the finite element analysis results. The experimental test values of the stresses in the porous skeletal scaffolds of group A and group B are in the range of 160~220 MPa. A15 produced the minimum compressive stress (-163.2 ± 16.9 MPa) when the Y-axis was used as the construction direction, while B15 produced the maximum compressive stress (-213.18 ± 21.89 MPa) when the Z-axis was used as the construction direction. The reason is presumed as follows: due to the characteristics of layer-by-layer molding of SLM, when the Y-axis is the construction direction,

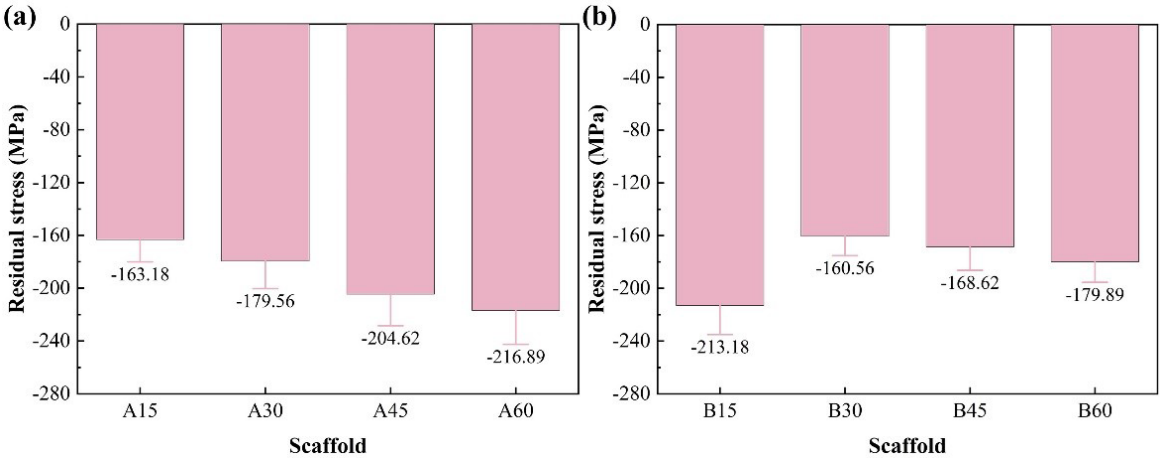

Figure 4. Experimental test values of residual stresses in different structures of NRHH porous skeletal scaffolds (a) Group A porous skeletal scaffolds, (b) Group B porous skeletal scaffolds.

the transverse strut is molded first and then the radial strut is molded, and the radial strut and the transverse strut have a larger angle when the θ angle is smaller, so the stress is released and diffused, and thus there is less stress, and the larger the θ angle, the strut undergoes a more complex thermal cycle and thus introduces a larger residual stress; in the case of the Z-axis, the radial strut is molded first and then the transverse strut is molded. When built in the Z-axis, the radial strut is formed first and then the transverse strut is formed, the radial strut of B15 is shorter, and there is frequent alternation between the radial strut and the transverse strut, which undergoes frequent laser energy transformations, resulting in an increase in residual stresses

Figure 5 shows the final residual deformation cloud map of the NRHH porous skeletal scaffolds, and the results show that, when the porous skeletal scaffolds formed with the Y-axis as the construction direction in group A were formed, the transverse struts on the left and right sides of the scaffolds were in an unconstrained state, and buckling deformation occurred, and the buckling of the left and right sides of the scaffolds intensified and the deformation amount increased as the θ-angle increased and the length of the transverse strut increased, with the A15 generating the minimum residual deformation, and A60 The maximum residual deformation is generated in A15 and A60, and the amount of deformation increases from 0.008 mm to 0.085 mm. In group B, the porous skeletal stent is formed with the Z-axis as the construction direction, and the maximum deformation occurs in the radial stent formed in the second and third layers, and the bottom of the stent is unsupported when it is formed at this time, and the laser energy beam leads to the melting of the metal powder to produce a molten pool that is subsided by the effect of gravity, which leads to residual deformation of the stent, and the amount of deformation is 0.008 mm for the different structures. The residual deformation of the pillar occurs, and the deformation amounts between different structures are 0.020 mm, 0.022 mm, 0.017 mm, 0.024 mm, respectively, with no obvious difference.

3.2. Forming quality and surface roughness

Figures 6 and 7 show the SEM images of SLM-prepared Group A and Group B NRHH porous skeletal scaffolds, respectively, where (e) and (f) are localized magnified images of (a) and (c), respectively. A clear reentrant hexagonal honeycomb profile with regular shape of the aperture can be observed from the images. It was also found that A15 and A30 porous skeletal scaffolds had good molding quality, while A45 and A60 porous skeletal scaffolds formed a large number of irregular deposits on the lower surface of the struts, and the scaffolds exhibited poor molding quality. Compared with the porous skeletal scaffolds in group A, powder adhesion and deposition were more severe in group B, which exhibited poorer forming quality. In group B, B15 exhibits the worst forming quality, and very obvious deposition is observed on the lower surface, B60 exhibits the optimal forming quality, and the forming quality of group B scaffolds is rather improved with the decrease of pillar deposition with the increase of θ angle. It can be concluded from the above analysis that when the porous skeletal scaffolds are formed with the Y-axis as the construction direction, the smaller the θ-angle is, the better the forming quality is, while when the scaffolds are formed with the Z-axis as the construction direction, on the contrary, the larger the θ-angle is, the better the forming quality is, which precisely indicates that the forming quality is related to the Poisson's ratio of the scaffolds, and with the Poisson's ratio becoming more and more negative, the porous skeletal scaffolds show better forming quality.

Figure 8 shows the surface morphology of the eight NRHH porous skeletal scaffolds obtained by laser spectroscopic confocal microscopy (the colors only indicate the relative heights), and the rougher strut surfaces were observed. The porous skeletal scaffolds shaped in group A had a relatively uniform height, while the porous skeletal scaffolds shaped in group B formed a larger melt pool at the intersection of the tilted struts due to the repeated melting-cooling of the powders at the intersection of the tilted

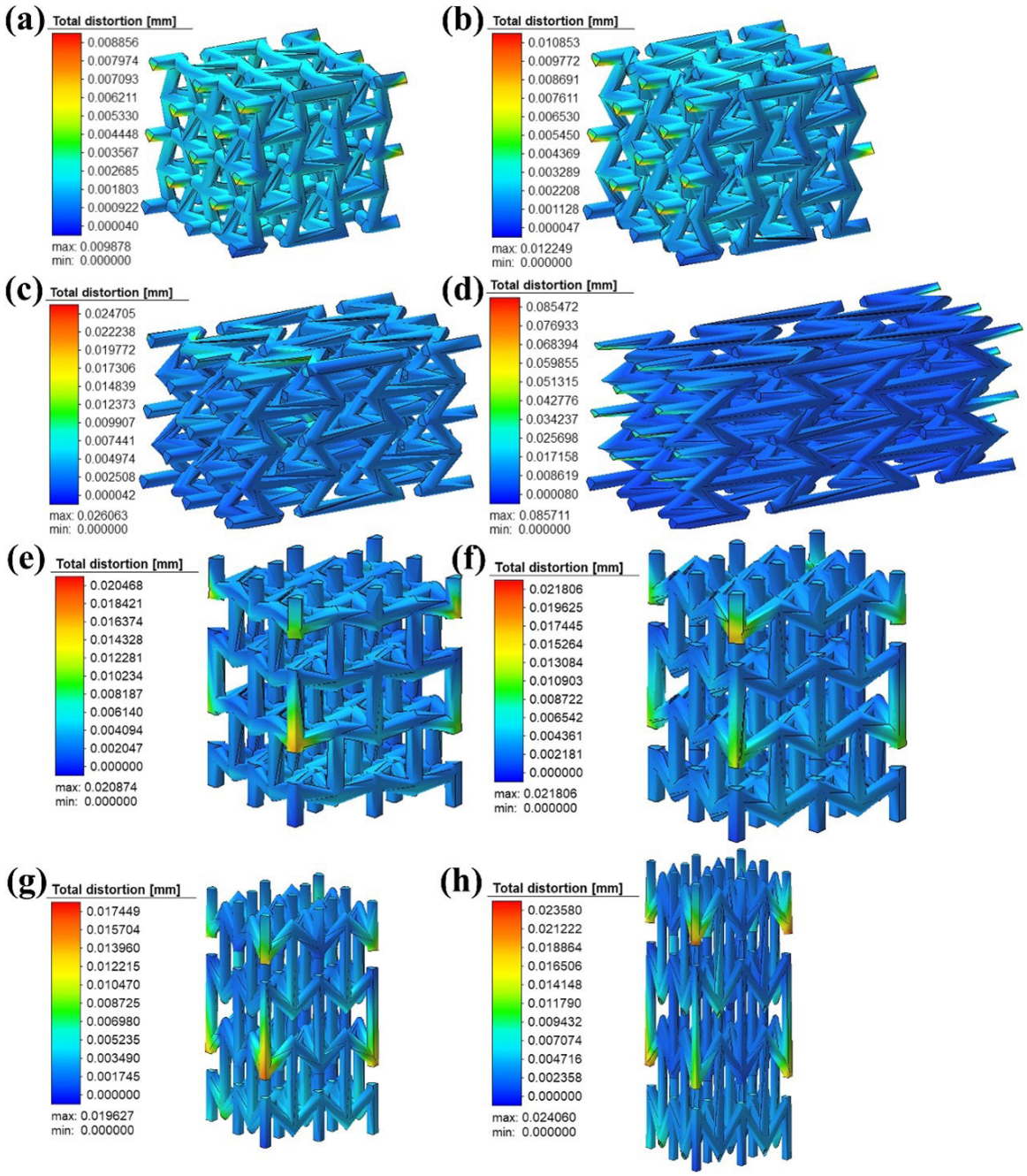

Figure 5. Final deformation cloud of NRHH porous skeletal scaffolds with different structures (a) A15, (b) A30, (c) A45, (d) A60, (e) B15, (f) B30, (g) B45, (h) B60.

struts during the shaping, which also proved that group A had a higher height compared with radially formed struts. The porous skeletal scaffolds formed in group B have a relatively high height compared with the radially formed pillars due to the repeated melting-cooling of powder at the intersection of the inclined pillars during forming, resulting in a significant height difference, which also proves that the porous skeletal scaffolds in group A have a better molding quality than those in group B.

Different structural designs have different forming paths and melt pool morphologies, thus exhibiting different surface line roughness, so roughness tests were conducted on the middle part of the transverse strut Ra1 and radial strut Ra2 to characterize the degree of concavity and convexity of the surface of the scaffolds, respectively, and the measurement locations are shown in Figure 8, the roughness curves are shown in Figure 9, and the statistical results are shown in Figure 10. From the statistical results, it can be seen that

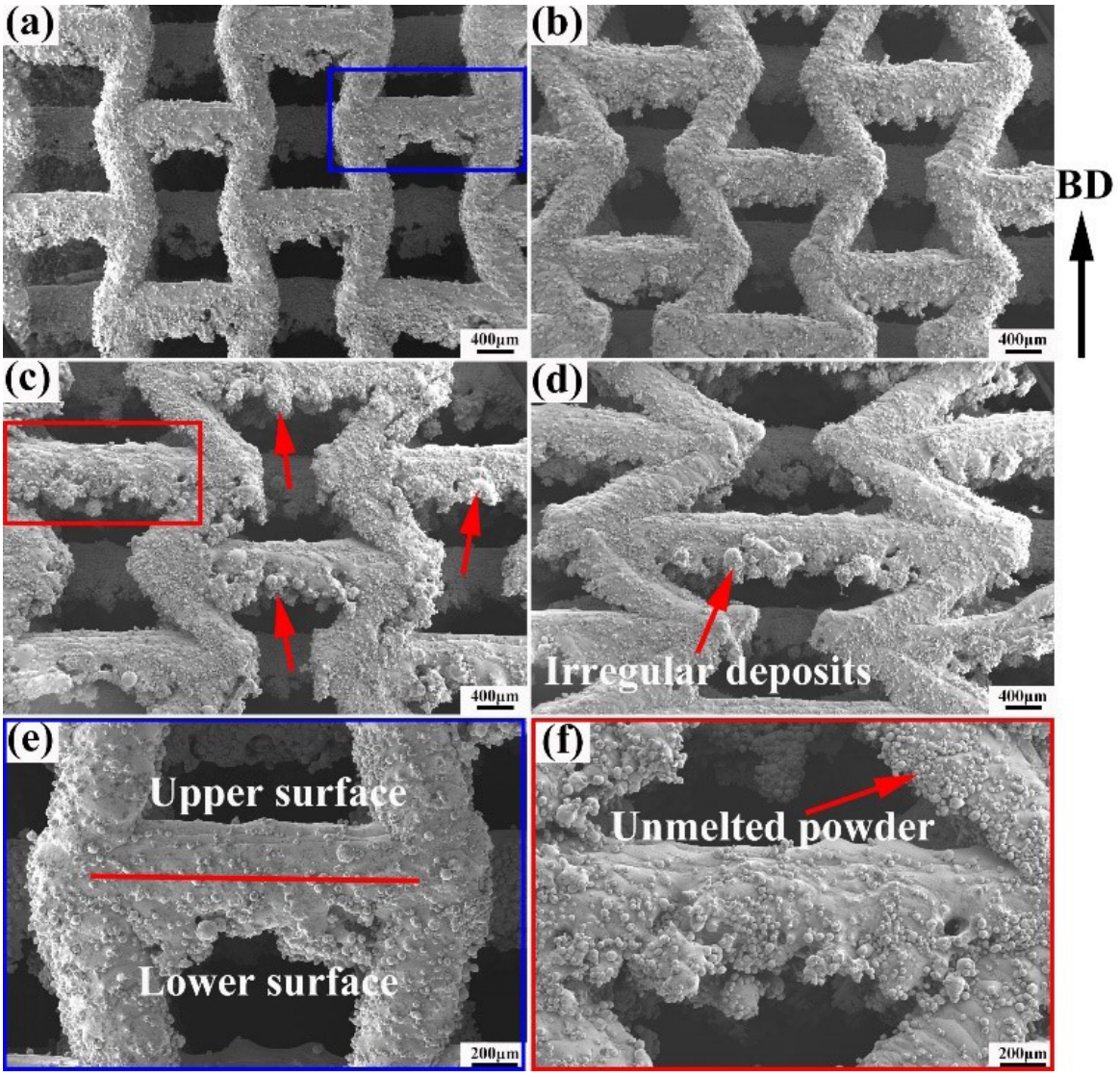

Figure 6. SEM images of different structures of NRHH porous skeletal scaffolds in group A. (a) A15, (b) A30, (c) A45, (d) A60, (e) Enlarged image of A15, (f) Enlarged image of A45 (the direction of the arrow pointed by the BD arrow is the construction direction).

the surface line roughness of the porous skeletal scaffolds in group B was much larger than that of group A. The average surface line roughness of group A was in the range of 8-24 μm, and that of group B was in the range of 14-57 μm, which was attributed to the more pronounced powder adhesion and deposition occurring in the scaffolds of group B. The surface line roughnesses of group A and group B showed different trends, with group A's average surface line roughness, Ra, increasing with the increase in θ angle and increased with increasing θ angle, the A15 porous skeletal scaffolds had the smallest Ra values with Ra1 and Ra2 of 8.9 μm and 14.8 μm, respectively, and Ra1 and Ra2 of A60 were 21.0 μm and 23.6 μm, respectively, which were reduced by 57.5% and 37.3% compared with that of A60; in Group B, the Ra decreased with increasing θ angle, and Ra1 and Ra2 of the B15 porous skeletal scaffolds were 54.6 μm and 47.3 μm for B15 and 34.1 μm and 14.5 μm for B60, respectively, and the B15 porous skeletal scaffold exhibited the largest surface line roughness.

The presence of adherent powder and irregular deposition on the struts resulted in lower actual porosity than theoretical porosity. The density of the NRHH porous skeletal scaffolds actually prepared by SLM was measured by Archimedes' method and the actual porosity obtained is shown in Figure 11. The designed theoretical porosity is 75%, and the actual porosity of the prepared porous skeletal scaffolds is lower than the theoretical porosity, and the porous skeletal scaffolds in group B are significantly lower than those in group A due to more serious powder adhesion and deposition, which results in a significantly lower porosity than those in group A. The porous skeletal scaffolds in group A decrease with increasing θ angle, and the porous skeletal scaffolds in group B increase with increasing θ angle, in which the actual porosity of A15 is the closest to the theoretical porosity.

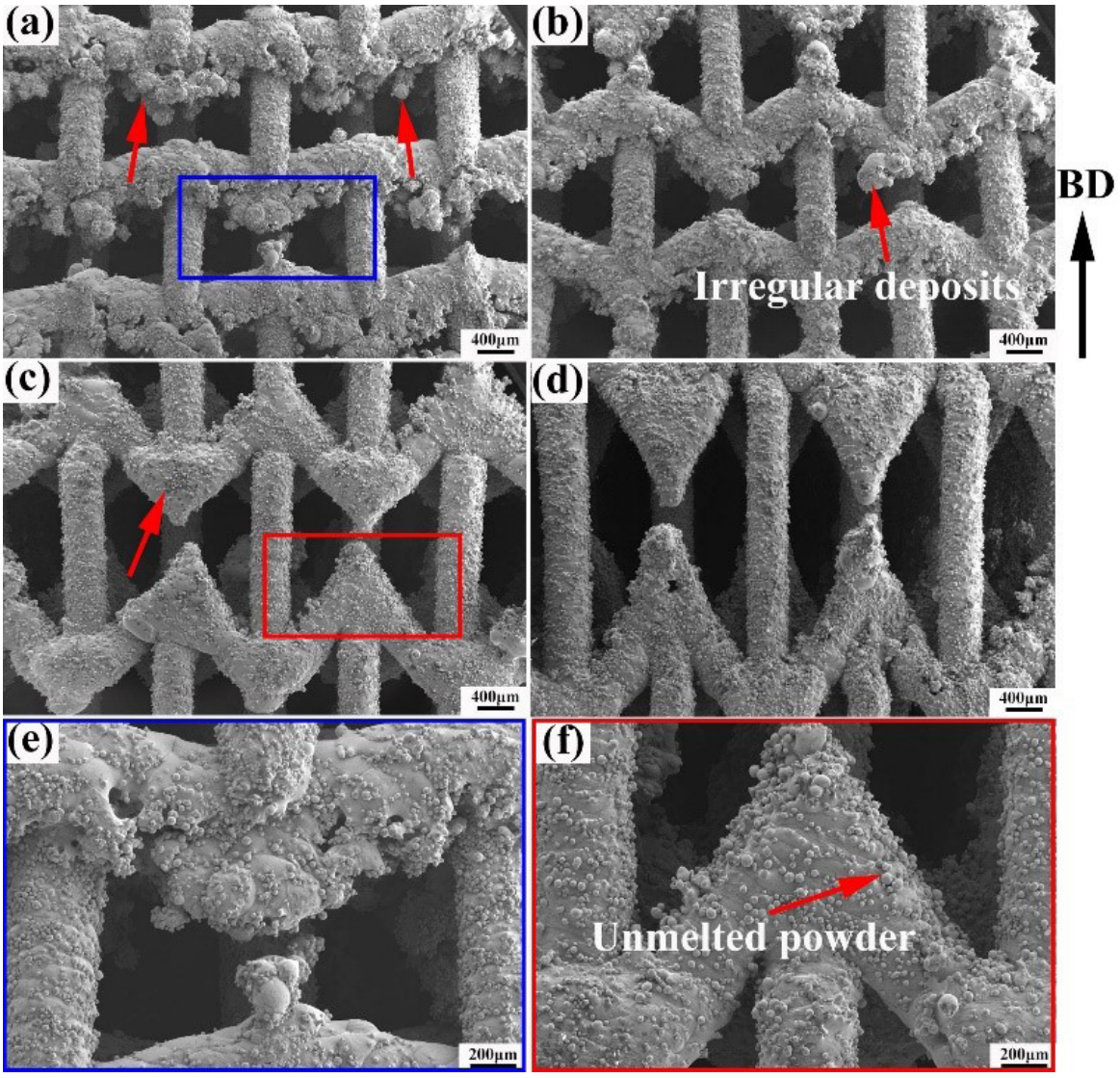

Figure 7. SEM images of different structures of NRHH porous skeletal scaffolds in group B: (a) B15, (b) B30, (c) B45, (d) B60, (e) enlarged image of B15, and (f) enlarged image of B45 (the direction of the BD arrow points to the direction of construction).

3.3. Compressive properties

Figure 12 shows the stress distribution cloud obtained from eight different structural porous skeletal scaffolds simulated by Ansys static mechanics. For group A NRHH porous skeletal scaffolds shaped with the Y-axis as the construction direction, the maximum stress value decreases after the θ angle decreases, and the maximum concentrated stress decreases from 1788.3 MPa to 300.6 MPa from A60 to A15 structural porous skeletal scaffolds, a reduction of 83.2%, which indicates that the compressive performance of the scaffolds is greatly enhanced with the decrease of the θ angle, and the stresses are concentrated in the middle of radially tilted struts. This shows that as the θ angle decreases, the compressive performance of the brace is greatly enhanced, and the stress is mainly concentrated in the middle part of the radial tilted strut, and the force on the transverse strut is shear force, which shares the stress at both ends of the radial strut and is used to resist the deformation of the radial strut, thus resulting in the stress distribution of the tilted strut which is small in the middle. As the θ angle increases, the tilt angle of vertical strut becomes smaller, and the stress sharing of transverse strut increases, which improves the stress concentration phenomenon of the stent, and the compression resistance of the stent is greatly enhanced. Group B NRHH porous skeletal stents formed with the Z-axis as the construction direction produced similar stress values after compression, and the radial struts of this group of porous skeletal stents played a major role in bearing the stress in the range of 497.8 MPa~534.8 MPa, but the maximum stress occurred in the middle of the transversely tilted struts, and there was an obvious stress concentration phenomenon, in which the stress concentration of the B60 porous skeletal stent was more obvious, indicating that its load-bearing capacity

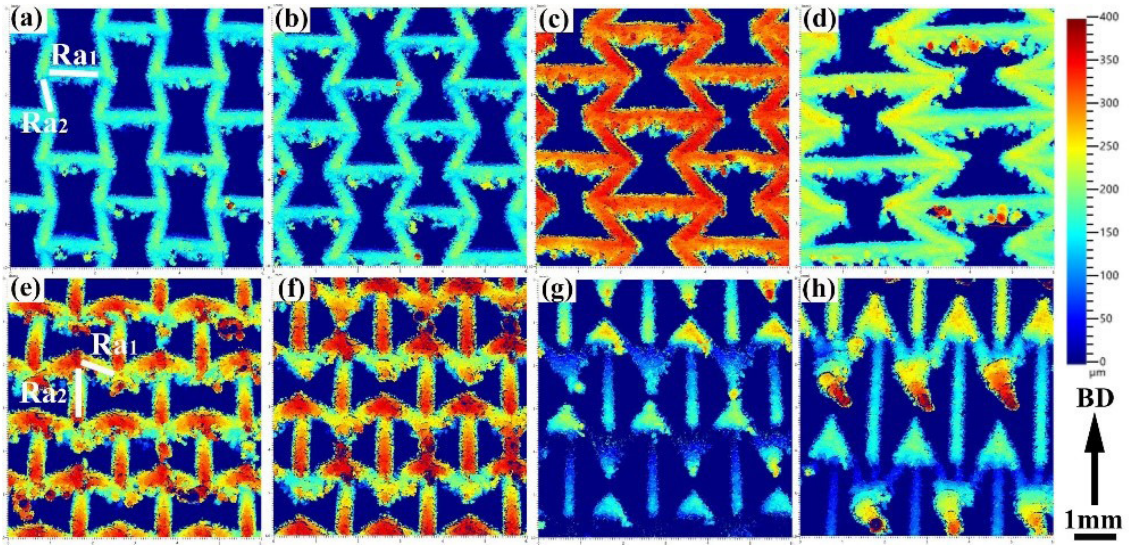

Figure 8. Surface topography of NRHH porous skeletal scaffolds (a) A15, (b) A30, (c) A45, (d) A60, (e) B15, (f) B30, (g) B45, and (h) B60 (the direction indicated by the arrow of BD is the direction of construction) direction is the direction of construction).

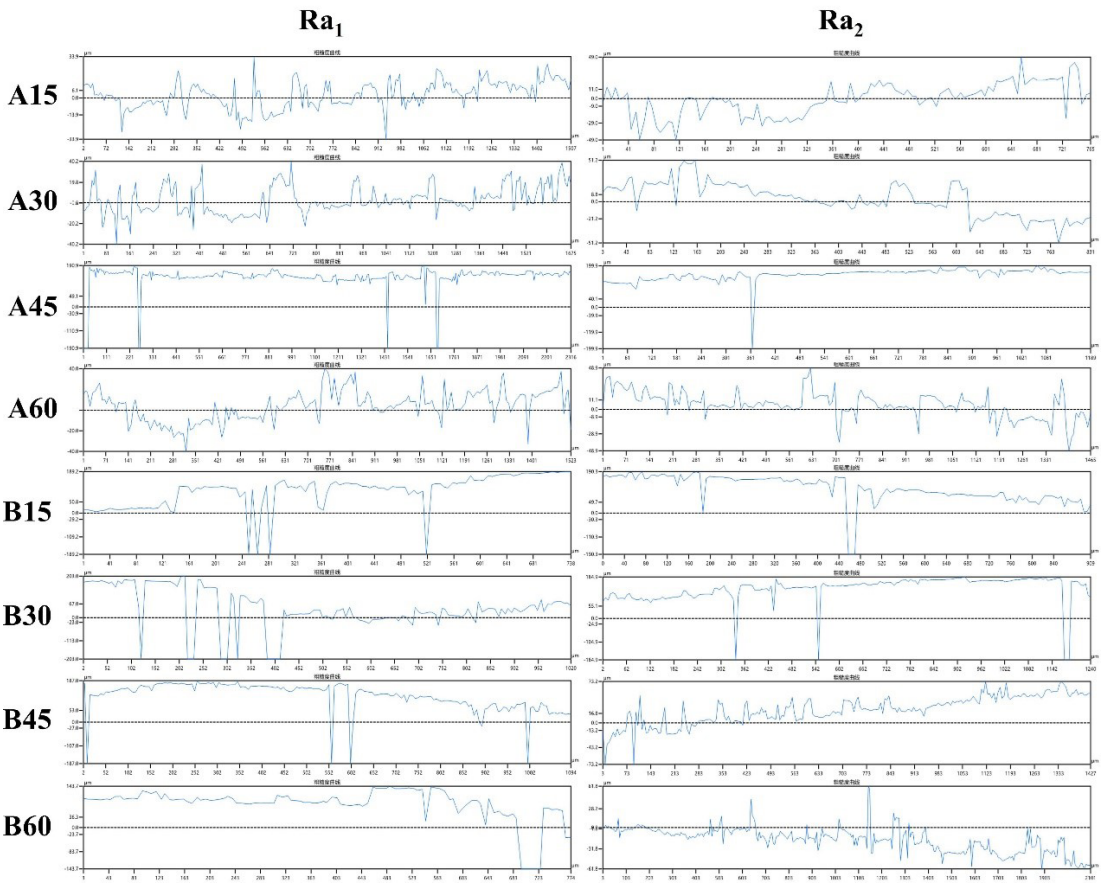

Figure 9. Surface line roughness curves of porous skeletal scaffolds with different structures of NRHH.

after implantation was greatly enhanced. This indicates that its load-bearing capacity after implantation is insufficient and is not conducive to prolonging the implantation life.

Figure 13 shows the deformation cloud diagram of the porous skeletal scaffolds after compression, unlike the conventional structure, the central part of the porous

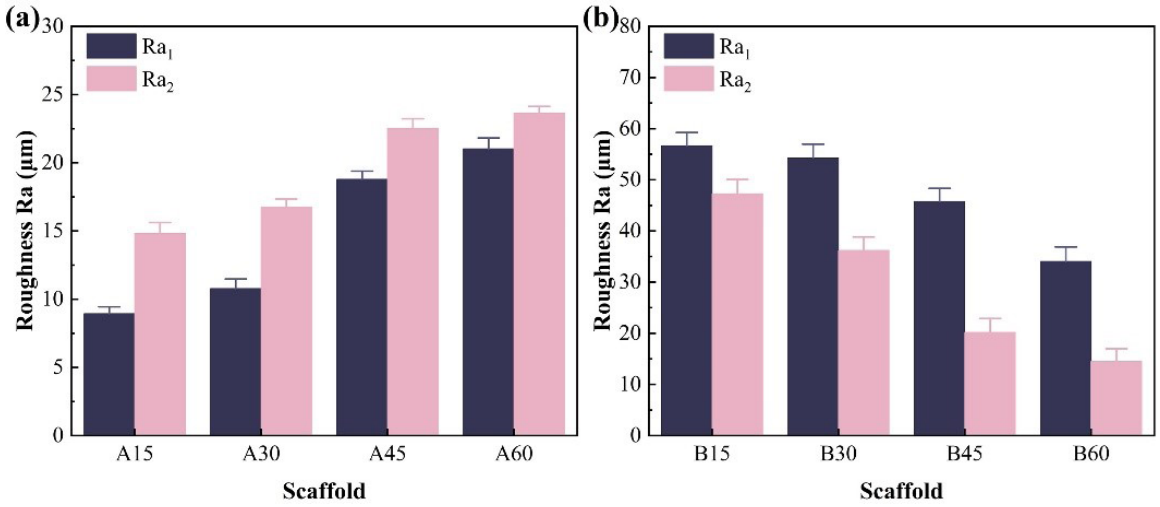

Figure 10. Trend of surface line roughness of NRHH porous skeletal scaffolds with structural design.

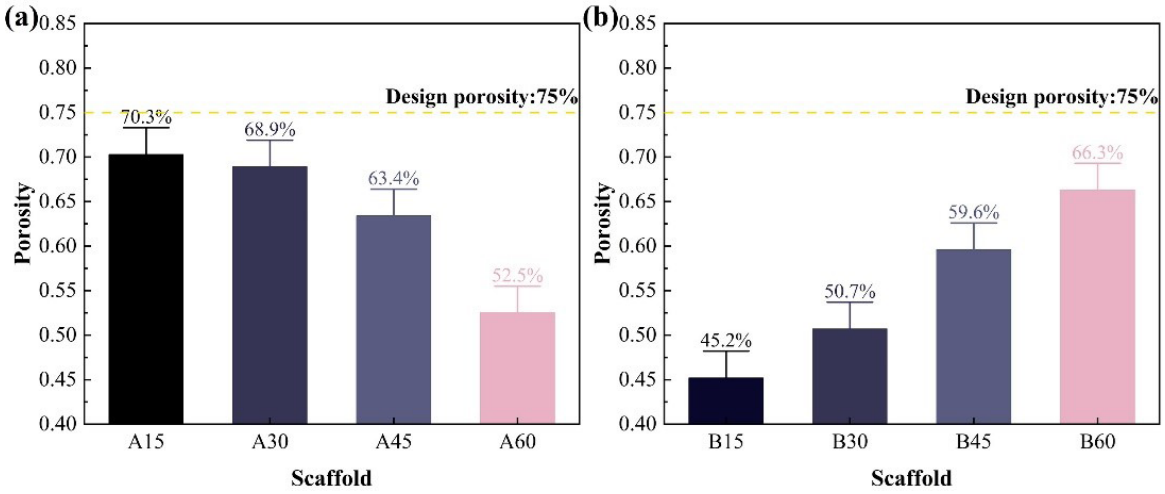

Figure 11. Porosity of porous skeletal scaffolds with different structures of NRHH.

skeletal scaffolds tends to contract transversely, thus generating additional shear stresses in the cross-section perpendicular to the direction of compression, and the porous skeletal scaffolds of group A are inwardly concave in the axial direction after being compressed in the radial direction with a pronounced negative Poisson's ratio characteristic, and the total deformation increases with the increase in the θ-angle, and the collapsing of the A45 and A60 porous skeletal scaffolds is obviously, and the strut aggregation occurred, while the A15 porous skeletal scaffold strut was more supportive and deformed to a lesser extent. The outermost radial strut of the porous skeletal stent in group B, on the other hand, produces serious deformation, with smaller differences between different structures, from which it can also be concluded that it is affected by the edge effect during the actual compression process, and its actual Poisson's ratio deviates from the theoretical Poisson's ratio to a certain extent.

Eight different structures of NRHH porous stents formed by SLM were compressed and the compression pressure-strain curves are shown in Figure 14. The compression process of the stent is divided into elastic deformation stage, plastic deformation stage and compaction stage. The porous stents with different structures showed different compression skills. Group A NRHH porous skeletal stent shaped in the construction direction of Y-axis, in the elastic deformation stage, A60 shows the highest compressive strength; into the plastic deformation stage from the contraction side began to appear deformation and distortion, the aperture diameter is gradually reduced, with the increase of strain, the trend of the growth of the stress decreases, and at this time, A15 shows the highest compressive strength; when the contraction to a certain extent, the stress reaches the highest value after the stent produces cracks, the stress begins to decline, the smaller the θ angle the greater the stress decline, at this time the stress of A15 rapidly decreases thus A30 exhibits

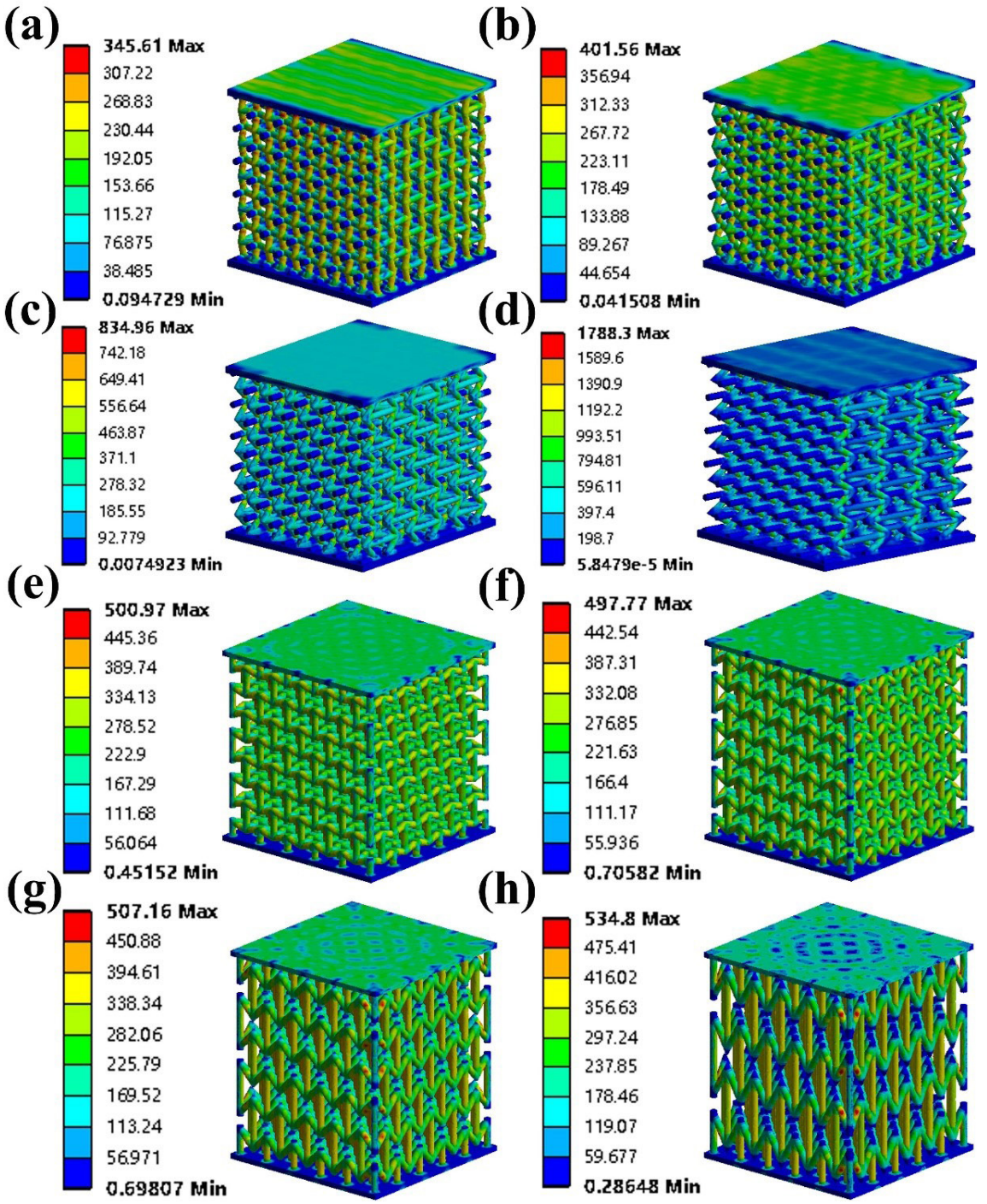

Figure 12. Stress distribution for static mechanical simulations of NRHH porous skeletal scaffolds with different structures (a) A15, (b) A30, (c) A45, (d) A60, (e) B15, (f) B30, (g) B45, (h) B60.

the highest compressive strength, and the porous skeleton scaffold enters the collapse stage. The NRHH porous skeletal scaffolds of group B formed with Z-axis as the construction direction, the larger the θ angle is, the larger the slope of the stress-strain curve is and the faster the stress increases in the elastic deformation stage and the plastic deformation stage; in the collapse stage, the different structures show different trends, the B15 and B30 porous skeletal scaffolds show a stress plateau, whereas the B45 and B60 porous skeletal scaffolds show a sawtooth-shaped curve, because the B45 and B60 porous skeletal scaffolds collapsed layer by layer during the compression process, and the damage

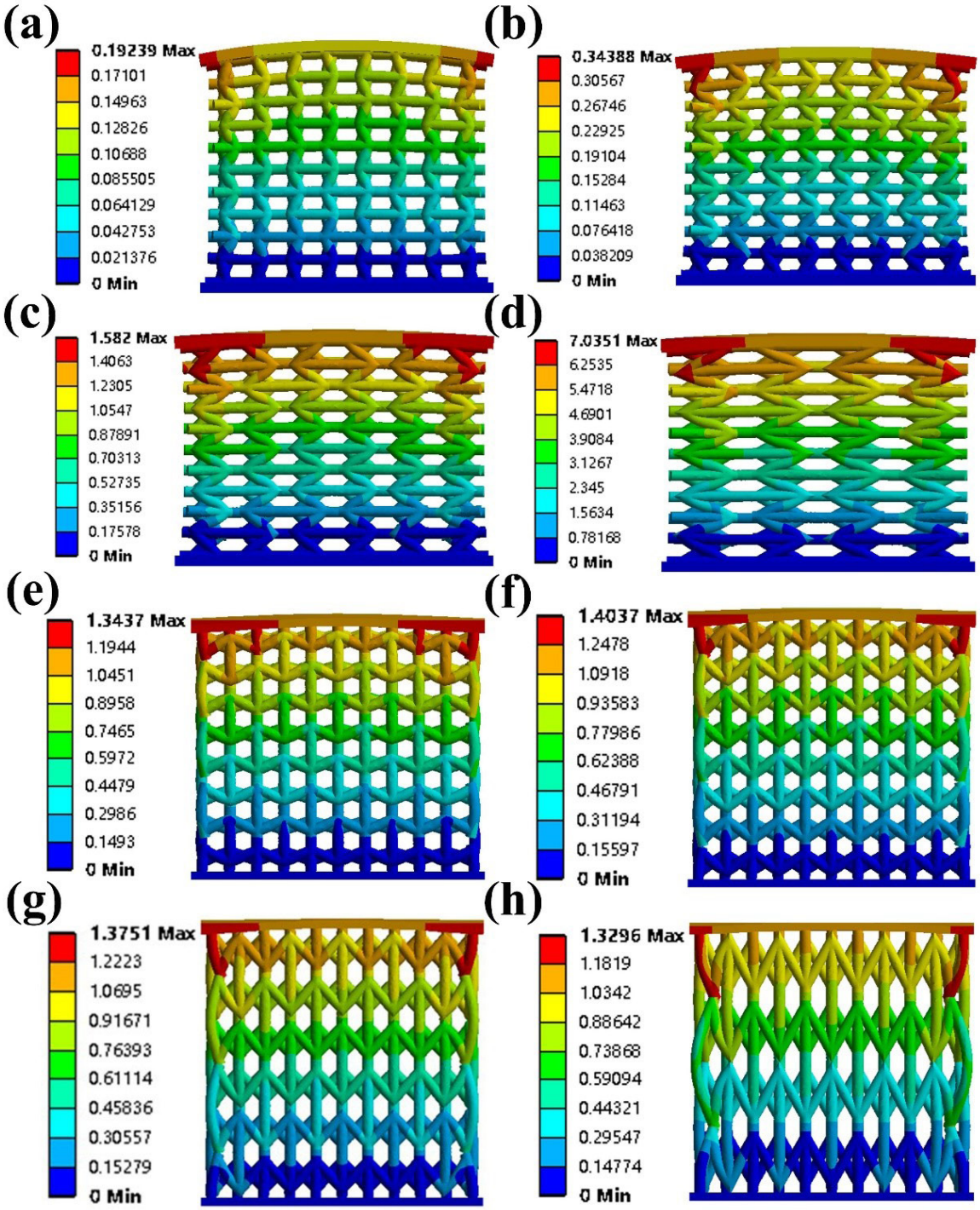

Figure 13. Deformation cloud for static mechanical simulations of NRHH porous skeletal scaffolds with different structures (a) A15, (b) A30, (c) A45, (d) A60, (e) B15, (f) B30, (g) B45, (h) B60.

occurred in the same layer of struts perpendicular to the direction of compression, the porous skeletal scaffolds were compressed until the whole layer collapsed, and then the next layer began to bear the load until collapse, the jagged curve in the stress-strain curve that corresponds to the number of cycles in the stress-strain curve corresponds to the collapse process of each layer of the porous skeletal stent, and the number of cycles is the same as the number of layers of the stent. Taking B45 as an example, its deformation after compression is shown in Figure 15.

The results of the elastic modulus of the NRHH porous skeletal scaffolds with different structures are shown in

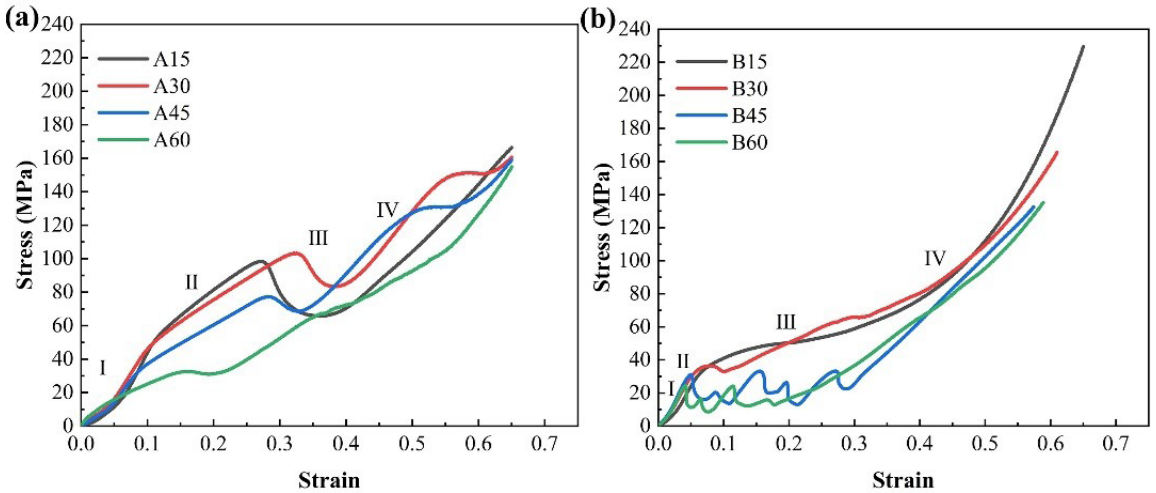

Figure 14. Compressive stress-strain curves of NRHH porous skeletal scaffolds with different structures.

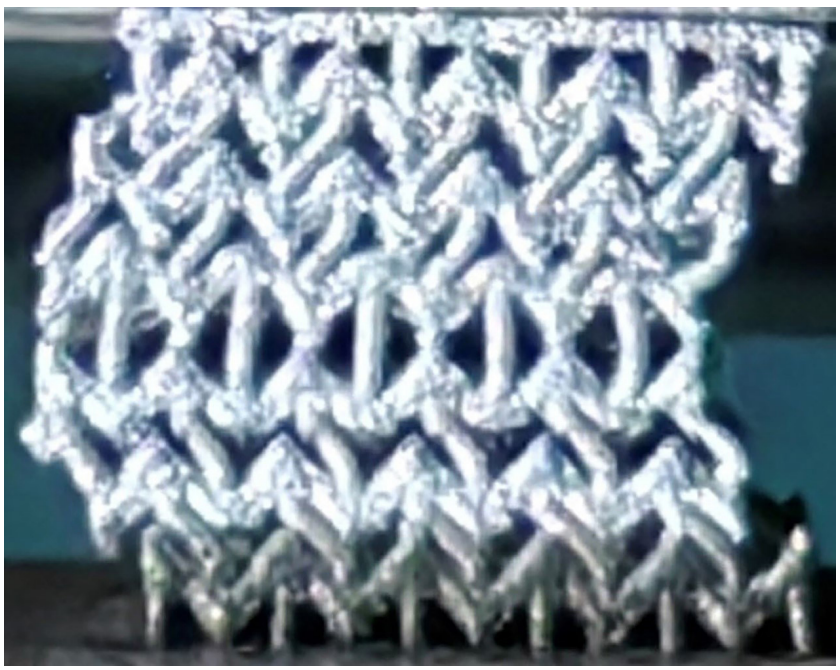

Figure 15. Layer collapse during compression of porous skeletal supports.

Figure 16, calculated as shown in Equation (3.1), and their elastic modulus meets the requirements of cancellous bone. The elastic modulus of the porous skeletal scaffolds of group A decreases with the increase of θ angle and is in the range of 0.2-0.8 GPa, and the maximum stress before collapse also decreases with the increase of θ angle, and A30 porous skeletal scaffolds show the highest pre-collapse stress, with a value of 103.2 MPa, and when the θ angle was increased to 45° and 60°, the maximum stress before collapse decreased significantly to 77.3 MPa and 32.3 MPa, respectively. The maximum stress before collapse of the porous skeletal scaffolds of group B decreased with the increase of the θ angle, and was in the range of about 20~50 MPa, which was lower compared with that of group A. The elastic modulus of the scaffolds also decreased with the increase of the θ angle, with a value in the range of 0.5~0.7 GPa range.

$$E = \frac{\sigma}{\varepsilon} \tag{3.1}$$

where E is the modulus of elasticity, σ is the stress and ε is the strain.

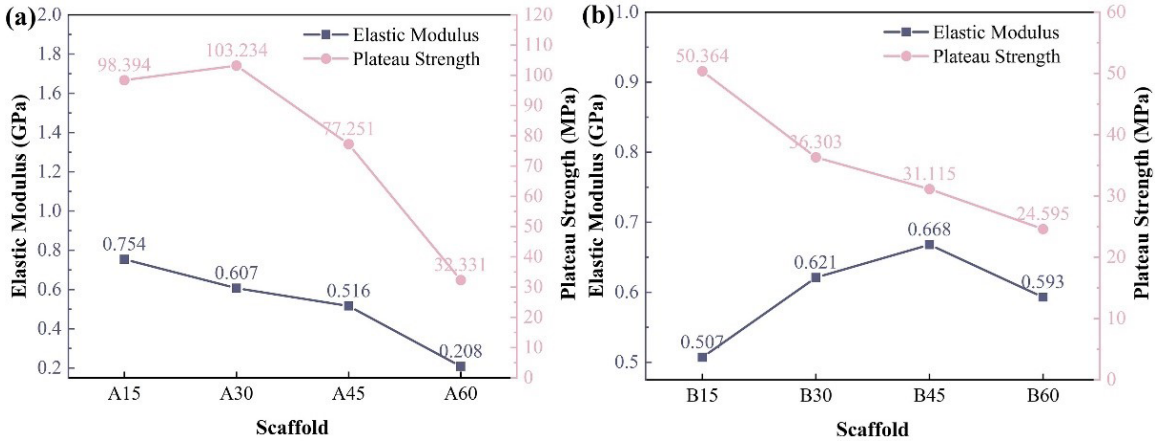

Figure 16. Modulus of elasticity and pre-collapse maximum stress values for different structures of NRHH porous skeletal scaffolds.

4. Conclusions

In this paper, porous skeletal scaffolds with four different reentry angles (15°, 30°, 45°, and 60°) were designed based on the reentrant hexagonal honeycomb structure (NRHH) and were formed by SLM with the Y-axis and Z-axis as the construction directions, respectively, and the residual stresses, molding qualities, surface roughness, and mechanical properties of the eight prepared NRHH porous skeletal scaffolds were characterized in search of the optimal structural design. The results show that the 15°-NRHH porous skeletal scaffold (A15) formed with the Y-axis as the construction direction has low elastic modulus and high compressive strength, and has the best performance compared with other scaffold structures.

1. The A15 porous skeletal scaffold produced the minimum residual stress (163.2 ± 16.9 MPa) and the minimum residual deformation, and the residual stress introduced by the porous skeletal scaffold when the Y-axis was used as the construction direction increased with the θ -angle, and when the θ -angle was increased to 60° the residual stress increased to 216.9 ± 25.6 MPa, whereas the B15 produced the maximum residual stress when the Z-axis was used as the construction direction.

2. The A15 and A30 porous skeletal scaffolds have good forming quality when the Y-axis is used as the construction direction, whereas the B15 has the worst forming quality when the Z-axis is used as the construction direction, and the B60 exhibits the optimal forming quality. In addition, the A15 structure has optimal forming quality, low surface roughness, and actual porosity close to the theoretical porosity.

3. The poorer forming quality directly leads to stress concentration and thus compressive resistance, and the porous skeletal scaffolds with greater negative Poisson's ratio are more resistant to shear deformation. The elastic modulus of the porous skeletal scaffolds decreases with the increase of θ -angle when the Y-axis is used as the construction direction, and the platform strength also decreases from 98.4 MPa to 32.3 MPa, which is a decrease of 67.2% with the increase of θ -angle. The modulus of elasticity of the porous skeleton scaffolds with Z-axis as the construction direction increases with the increase of θ angle, and the platform strength decreases with the increase of θ -angle.

5. Acknowledgments

This study was supported by the Science and Technology Enterprise Innovation Program of Shandong Province China (2024TSGC0954, 2024TSGC0410, 2024TSGC0907, 2024TSGC0462 and 2024TSGC0041).

6. References

1. Wang S, Shi ZA, Liu L, Zhou X, Zhu L, Hao Y. The design of Ti6Al4V Primitive surface structure with symmetrical gradient of pore size in biomimetic bone scaffold. Mater Des. 2020;193:108830. http://doi.org/10.1016/j.matdes.2020.108830.
2. Bulygina I, Senatov F, Choudhary R, Kolesnikov E, Kaloshkin S, Scholz R, et al. Biomimetic scaffold fabricated with a mammalian trabecular bone template. Polym Degrad Stabil. 2020;172:109076. http://doi.org/10.1016/j.polymdegradstab.2020.109076.
3. Zadpoor AA. Mechanical meta-materials. Mater Horiz. 2016;3(5):371-81. http://doi.org/10.1039/C6MH00065G.
4. Choudhry NK, Panda B, Kumar S. In-plane energy absorption characteristics of a modified re-entrant auxetic structure fabricated via 3D printing. Compos, Part B Eng. 2022;228:109437. http://doi.org/10.1016/j.compositesb.2021.109437.
5. Clausen A, Wang F, Jensen JS, Sigmund O, Lewis JA. Topology Optimized Architectures with Programmable Poisson's Ratio over Large Deformations. Adv Mater. 2015;27(37):5523-7. http://doi.org/10.1002/adma.201502485. PMid:26291030.
6. Schaedler TA, Jacobsen AJ, Torrents A, Sorensen AE, Lian J, Greer JR, et al. Ultralight metallic microlattices. Science. 2011;334(6058):962-5. http://doi.org/10.1126/science.1211649. PMid:22096194.
7. Zheng X, Lee H, Weisgraber TH, Shusteff M, Deotte J, Duoss EB, et al. Ultralight, ultrastiff mechanical metamaterials. Science. 2014;344(6190):1373-7. http://doi.org/10.1126/science.1252291. PMid:24948733.
8. Ren X, Das R, Tran P, Ngo TD, Xie YM. Auxetic metamaterials and structures: a review. Smart Mater Struct. 2018;27(2):023001. http://doi.org/10.1088/1361-665X/aaa61c.
9. Yang L, Cormier D, West H, Harrysson O, Knowlson K. Non-stochastic Ti–6Al–4V foam structures with negative Poisson's ratio. Mater Sci Eng A. 2012;558:579-85. http://doi.org/10.1016/j.msea.2012.08.053.

10. Ji S, Li L, Motra HB, Wuttke F, Sun S, Michibayashi K, et al. Poisson's ratio and auxetic properties of natural rocks. J Geophys Res Solid Earth. 2018;123(2):1161-85. http://doi.org/10.1002/2017JB014606.
11. Marmier A, Miller W, Evans KE. Negative Poisson's ratio: a ubiquitous feature of wood. Mater Today Commun. 2023;35:105810. http://doi.org/10.1016/j.mtcomm.2023.105810.
12. Lethbridge ZAD, Walton RI, Marmier ASH, Smith CW, Evans KE. Elastic anisotropy and extreme Poisson's ratios in single crystals. Acta Mater. 2010;58(19):6444-51. http://doi.org/10.1016/j.actamat.2010.08.006.
13. Andrew JJ, Schneider J, Schiffer A, Hafeez F, Kumar S. Dynamic crushing of tailored honeycombs realized via additive manufacturing. Int J Mech Sci. 2022;219:107126. http://doi.org/10.1016/j.ijmecsci.2022.107126.
14. Wang X-T, Wang B, Li X-W, Ma L. Mechanical properties of 3D re-entrant auxetic cellular structures. Int J Mech Sci. 2017;131-132:396-407. http://doi.org/10.1016/j.ijmecsci.2017.05.048.
15. Balan PM, Mertens AJ, Raju Bahubalendruni MVA. Auxetic mechanical metamaterials and their futuristic developments: a state-of-art review. Mater Today Commun. 2023;34:105285. http://doi.org/10.1016/j.mtcomm.2022.105285.
16. Spadoni A, Ruzzene M. Elasto-static micropolar behavior of a chiral auxetic lattice. J Mech Phys Solids. 2012;60(1):156-71. http://doi.org/10.1016/j.jmps.2011.09.012.
17. Grima JN, Evans KE. Auxetic behavior from rotating squares. J Mater Sci Lett. 2000;19(17):1563-5. http://doi.org/10.1023/A:1006781224002.
18. Grima J N, Farrugia P-S, Gatt R, Attard D. On the auxetic properties of rotating rhombi and parallelograms: a preliminary investigation. Physica Status Solidi (b), 2008;245(3):521-9. https://doi.org/10.1002/pssb.200777705.
19. Evans KE, Nkansah MA, Hutchinson IJ. Auxetic foams: modelling negative Poisson's ratios. Acta Metall Mater. 1994;42(4):1289-94. http://doi.org/10.1016/0956-7151(94)90145-7.
20. Kolken HMA, Janbaz S, Leeflang SMA, Lietaert K, Weinans HH, Zadpoor AA. Rationally designed meta-implants: a combination of auxetic and conventional meta-biomaterials. Mater Horiz. 2018;5(1):28-35. http://doi.org/10.1039/C7MH00699C.
21. Chen D, Zheng X. Multi-material additive manufacturing of metamaterials with giant, tailorable negative Poisson's Ratios. Sci Rep. 2018;8(1):9139. http://doi.org/10.1038/s41598-018-26980-7. PMid:29904093.
22. Jiang Y, Li Y. 3D printed auxetic mechanical metamaterial with chiral cells and re-entrant cores. Sci Rep. 2018;8(1):2397. http://doi.org/10.1038/s41598-018-20795-2. PMid:29402940.
23. Jiang Y, Li Y. 3D Printed Chiral Cellular Solids with Amplified Auxetic Effects Due to Elevated Internal Rotation. Adv Eng Mater. 2017;19(2):1600609. http://doi.org/10.1002/adem.201600609.
24. Sing SL, Wiria FE, Yeong WY. Selective laser melting of lattice structures: A statistical approach to manufacturability and mechanical behavior. Robot Comput-Integr Manuf. 2018;49:170-80. http://doi.org/10.1016/j.rcim.2017.06.006.
25. Mondal P, Das A, Wazeer A, Karmakar A. Biomedical porous scaffold fabrication using additive manufacturing technique: porosity, surface roughness and process parameters optimization. International Journal of Lightweight Materials and Manufacture. 2022;5(3):384-96. http://doi.org/10.1016/j.ijlmm.2022.04.005.
26. Zhang Y, Sun N, Zhu M, Qiu Q, Zhao P, Zheng C, et al. The contribution of pore size and porosity of 3D printed porous titanium scaffolds to osteogenesis. Biomaterials Advances. 2022;133:112651. http://doi.org/10.1016/j.msec.2022.112651. PMid:35034817.
27. Gryko A, Prochor P, Sajewicz E. Finite element analysis of the influence of porosity and pore geometry on mechanical properties of orthopaedic scaffolds. J Mech Behav Biomed Mater. 2022;132:105275. http://doi.org/10.1016/j.jmbbm.2022.105275. PMid:35623106.
28. Deng F, Liu L, Li Z, Liu J. 3D printed Ti6Al4V bone scaffolds with different pore structure effects on bone ingrowth. J Biol Eng. 2021;15(1):4. http://doi.org/10.1186/s13036-021-00255-8. PMid:33478505.
29. Lu Y, Zhou Y, Liang X, Zhang X, Zhang C, Zhu M, et al. Early bone ingrowth of Cu-bearing CoCr scaffolds produced by selective laser melting: an in vitro and in vivo study. Mater Des. 2023;228:111822. http://doi.org/10.1016/j.matdes.2023.111822.
30. Chen Q, Thouas GA. Metallic implant biomaterials. Mater Sci Eng Rep. 2015;87:1-57. http://doi.org/10.1016/j.mser.2014.10.001.
31. Čapek J, Machová M, Fousová M, Kubásek J, Vojtěch D, Fojt J, et al. Highly porous, low elastic modulus 316L stainless steel scaffold prepared by selective laser melting. Mater Sci Eng C Mater Biol Appl. 2016;69:631-9. http://doi.org/10.1016/j.msec.2016.07.027. PMid:27612756.
32. Wieding J, Lindner T, Bergschmidt P, Bader R. Biomechanical stability of novel mechanically adapted open-porous titanium scaffolds in metatarsal bone defects of sheep. Biomaterials. 2015;46:35-47. http://doi.org/10.1016/j.biomaterials.2014.12.010. PMid:25678114.
33. Mercelis P, Kruth JP. Residual stresses in selective laser sintering and selective laser melting. Rapid Prototyping J. 2006;12(5):254-65. http://doi.org/10.1108/13552540610707013.